Alma Mater Studiorum Università di Bologna
Archivio istituzionale della ricerca

Photoelectrochemical oxidation of glycerol on hematite: thermal effects, in situ FTIR and long-term HPLC product analysis

Original Paper

Photoelectrochemical oxidation of glycerol on haematite: thermal effects, in situ FTIR and long-term HPLC product analysis

Nickson   Perini,   [1,2]

Cristian   Hessel,   [1,2]

José L.   Bott-Neto,   [2,3]

Cléo AQ1   T. G. V. M. T.   Pires,   [2,3]

Pablo S.   Fernandez,   [2,3]

Elton Sitta, [1,2]✉

Email esitta@ufscar.br

[1] Federal University of São Carlos, São Carlos, São Paulo, 13565-905 Brazil

[2] Center for Innovation on New Energies, Campinas, São Paulo, 13083-841 Brazil

[3] University of Campinas, -SP, Campinas, São Paulo, 13560-970 Brazil

AQ2

Abstract

Photoelectrochemical (PEC) oxidation of biomass is a profitable approach to produce hydrogen by substituting the water oxidation reaction in the electrolyzers' photoanodes. Among the biomass-derived molecules, glycerol becomes an interesting alternative to water since its standard thermodynamic potential is considerably lower than that of water and because it is widely produced in the biodiesel industry. Herein, we performed a fundamental study of the PEC oxidation of glycerol on haematite. In situ FTIR experiments and long-term electrolysis followed by HPLC analysis revealed C1, C2 and C3 oxidation products showing the low selectivity of the reaction under these conditions. We explained this lack of selectivity by an electrooxidation mechanism involving highly reactive radicals as intermediates.

Graphical abstract

AQ3
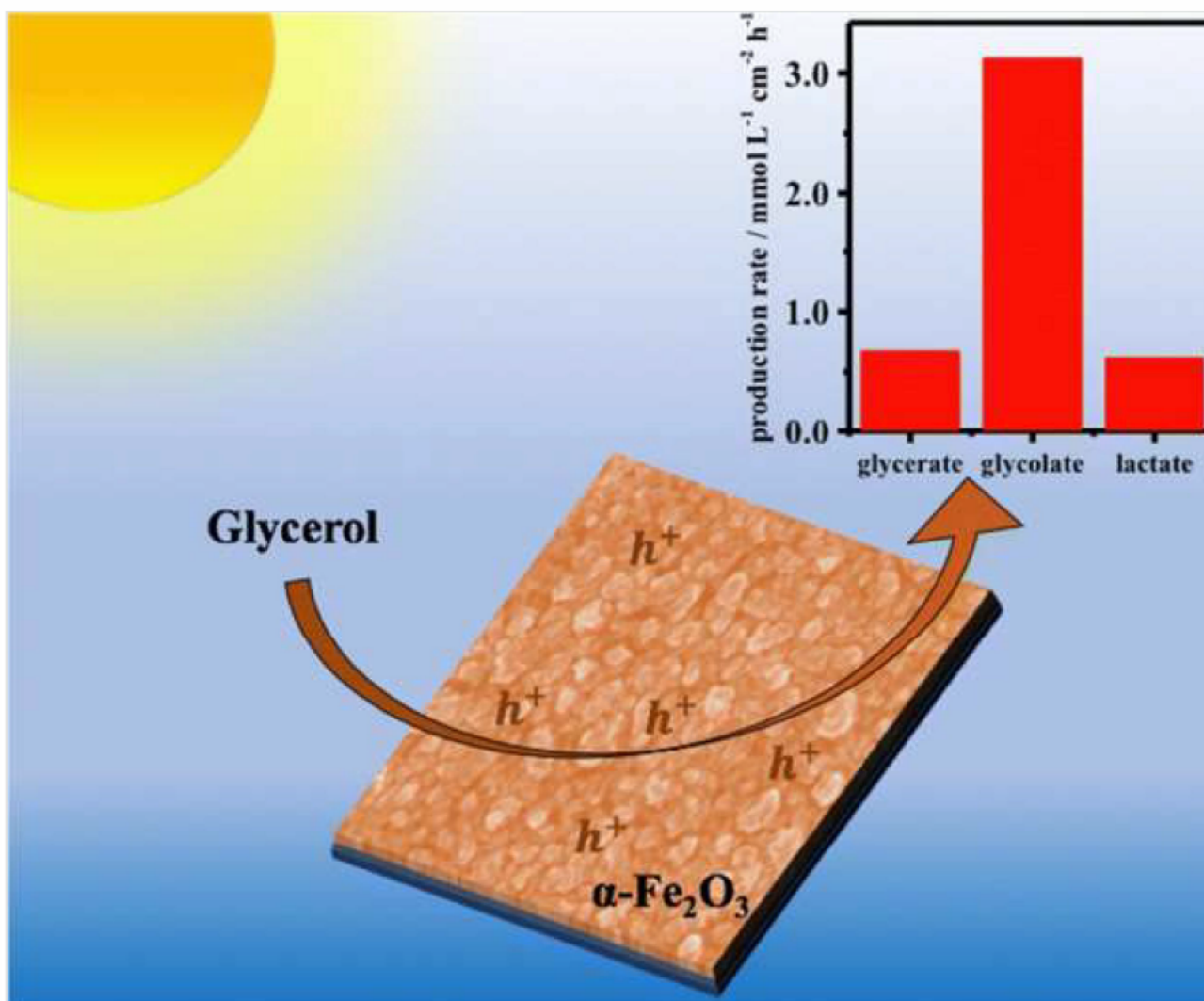
Keywords

Photoelectrochemical, Oxidation, Glycerol, Haematite

Supplementary Information

The online version contains supplementary material available at
https://doi.org/10.1007/s10008-020-04878-7.

Introduction

Photoelectrochemical (PEC) hydrogen production from biomass-derived
resources is a promising approach towards a more sustainable economy and

development [1]. When compared to the large literature of photocatalysis (PC) degradation of small organic molecules [1] and pollutants [2, 3] in aqueous effluents, the studies of organic PEC oxidation aiming hydrogen production have been lesser explored.

The presence of organic molecules such as methanol, [4] ethanol, [5] and glucose [6] in the electrolyte always increases the oxidation photocurrents at lower overpotentials, which is likely driven for the much lower standard potential for the complete electrochemical oxidation of several small organic molecules (around 0.0 V versus NHE) when compared to the oxidation of water (1.23 V versus NHE). Beyond acting as hole scavengers, organic molecules PEC oxidation provides an opportunity to produce chemical commodities, instead of oxygen, from biomass waste [7]. Thus, a huge number of biomass-derived molecules can be used for this purpose including alcohols [8], organic acid [9] and saccharides [10, 11]. Glycerol is a suitable option to feed the anode compartment of the PEC cell since it is obtained as a by-product of the biodiesel industry [12, 13, 14]. Furthermore, from the glycerol PEC oxidation (GPECO), it is possible to obtain value-added chemicals, such as dihydroxyacetone and glyceric acid [15].

Similar to PEC oxidation of several small organic molecules [10], TiO_2 [16, 17, 18, 19] is the most employed semiconductor for GPECO. Recently, Liu et al. [20] studied GPECO on $BiVO_4$ photoanodes and achieved 51% of dihydroxyacetone (DHA) selectivity after 1 h electrolysis at 1.2 V versus RHE in acidic (pH 2.0) electrolyte. Huang et al. [21] also using $BiVO_4$ as photoanode in borate buffer (pH 9.0) electrolyte obtained 15% of DHA and 85% of formic acid after 3 h of electrolysis at 0.70 V versus RHE.

Among the available photoactive materials, haematite (α-Fe_2O_3) is a very promising photoanode due to its high chemical stability, non-toxicity, abundance and a theoretical maximum efficiency of 12 mA cm ^{2}. Haematite has a 2.2 eV band gap enabling visible light absorption, but its performance to oxidize water is limited by the fast e $/h^+$ recombination [22, 23]. Haematite can be prepared using simple and low-cost methods such as Pechini/spin coating [24] and electrodeposition [25]. Among them, cathodic [26] and anodic [27] electrodeposition of metallic iron and iron oxyhydroxides, respectively, have the advantage of being scalable, easy thickness control and good film

adherence. Chong et al. [28] showed that nickel phosphate-modified α-Fe_2O_3 photoanodes are able to provide high GPECO rate at neutral pH but with low selectivity for glycerol oxidation products. Thus, in order to understand from a fundamental point of view the PEC oxidation of glycerol on α-Fe_2O_3, we studied the GPECO reaction pathways by in situ FTIR experiments and electrolysis coupled to HPLC analysis. The apparent activation energy was also estimated for several potentials and discussed in terms of organic radical formation.

Experimental

Synthesis of haematite photoanode

All chemicals were purchased from Sigma-Aldrich and used without further purification. α-Fe_2O_3 was prepared by iron electrodeposition in an aqueous electrolyte composed by 20 mL of 1.0 M NaOH, 2 mL of lactic acid and 30 mL of ethylene glycol followed by completion with ultra-pure water in a volumetric flask of 100 mL (MiliQ, 18.2 MΩ cm). Afterwards, the pH was corrected to 3.0 with H_2SO_4. The iron electrodeposition was performed on 1.0×1.0 cm FTO electrodes during the cyclic voltammogram from 0.80 V to 1.45 V versus Ag/AgCl/(KCl sat.) at 50 mV s^{-1}, using a cut-off charge of 4.0 °C cm^{-2} to control the iron mass onto FTO. The FTO/Fe samples were cleaned with pure water and immediately treated at 550 °C and 800 °C for 30 and 5 min, respectively, and cooled in air.

Physical characterizations

Powder XRD measurements were performed using a Shimadzu 6000 diffractometer operating at 30 kV/40 mA, with a copper tube: $\lambda k\alpha = 1.5418$ Å, in the range of 10 80° (2θ) and a sweep rate of 2° min^{-1}. Raman spectra were obtained using a micro-Raman spectrometer Horiba iHR550 coupled to a CCD detector operating with an argon-ion laser of 514.5 nm and a maximum power of 200 mW. UV-Vis measurements were carried out using a Varian Cary 5E in a range of 400 800 nm. The haematite thin films were analysed in the transmittance mode, with a clean FTO substrate as reference. SEM images were taken in a FEI inspect F50.

Photoelectrochemical experiments

Photoelectrochemical measurements were performed in a Teflon cell built with a quartz window. The simulated solar illumination was obtained from a 300 W Xenon lamp with an AM 1.5G filter (100 mW cm^{-2}), and the potential/current was controlled/measured with an Autolab PGSTAT 302N potentiostat. The working electrode was composed of the front-illuminated FTO/haematite films, and a platinum plate with a high surface area was used as counter-electrode and a reversible hydrogen electrode (RHE) build with the same electrolyte solution, 0.10 M KOH (pH 12.9), was used as a reference electrode. Ten voltammetry cycles from 0.45 to 1.60 V at 50 mV s^{-1} in oxygen-free electrolyte were performed as pre-treatment before all experiments.

In situ FTIRs

In situ Fourier transform infrared spectroscopy (FTIR) experiments were performed on a Shimadzu IR prestige-21 spectrometer equipped with a HgCdTe (MCT) detector and specular reflectance accessory adapted. The experiments were performed in dark and in the presence of light by using a 445 nm LED. To remove the CO_2 interference and water from the atmosphere the beam path was saturated with N_2 gas (5.0 N). Spectra were recorded from 0.40 to 1.40 V versus RHE every 100 mV during a stepped chronoamperometry (256 interferograms with a resolution of 4 cm^{-1}). More details about the experimental system can be found elsewhere [29]. The haematite photoanodes were synthesized onto polished glassy carbon (GC) electrode as described above for the FTO substrate. As the hydrogen evolution is more favourable on the GC electrode than FTO, the $FeSO_4$ concentration was increased in the electrolyte to 50 mM, to improve the efficiency in the Fe electrodeposition. The thermal treatment was performed at 450 °C for 30 min. As previously reported [30], the presence of tin in the FTO substrate segregated to the haematite phase during the thermal treatment and the incorporation of tin improves the haematite photo-activity. Therefore, to investigate the influence of tin content in the haematite photoanodes, 3.5 wt% of tin, using $SnSO_4$, was added to the deposition bath. Thus, the in situ FTIR experiment was performed on pure haematite and tin-modified haematite.

Sample collection and high-performance liquid

chromatography (HPLC)

Sample collection was performed after 4 h of electrolysis at 1.0 V versus RHE in a 5 mL Teflon cell equipped with a quartz window. In these experiments, the counter-electrode (working as a cathode in this case) was placed into a glass tube to avoid the reduction of the oxidation products. After the chronoamperometric experiments, 0.5 mL was collected and immediately neutralized with 0.5 mL of 0.05 M H_2SO_4 solution to avoid further chemical reactions due to the storage in strong alkaline media. HPLC measurements were performed in a Shimadzu LC-6AD chromatograph with a quaternary pump, a thermostatic column compartment CTO-20A, an UV vis (SPD-20AV at 205 and 254 nm), and a refractory index (RID-20A) detector, both kept at 40 °C. Four columns (one Aminex HPX87-H and three Shodex Sugar SH1011) were used with a Bio-Rad 1250131 precolumn, kept at 84 °C. The mobile phase was 0.5 mM H_2SO_4 with a flow rate of 0.6 mL min^{-1}, and the injection volume was 20 μL. To identify and quantify the obtained products, standards simulating the used electrolyte (0.1 M KOH + 0.05 M H_2SO_4 + 0.1 M glycerol) were prepared which were combined with possible glycerol oxidation products (sodium mesoxalate, oxalic acid, tartronic acid, hydroxypyruvic acid, glyoxylic acid, glyceric acid, glycolic acid, glyceraldehyde, formic acid, lactic acid and dihydroxyacetone). Product concentrations were determined by linear correlation with peak areas from the standards and the samples.

Results

Synthesis and structural characterization of haematite photoanode

Figure 1 presents the physical characterization of the haematite film. X-ray diffraction peaks in $2\theta = 24.16, 33.22, 40.94, 54.60, 62.46$ and 64.04 of haematite film (Fig. 1a) matches with the powder haematite diffraction pattern, confirming the formation of oxide (JCPDS 33 0664). Figure 1b insert shows the electrodeposited Fe in the metallic form (grey) and after the conversion to haematite (orange) (larger images can be found in the supplementary file section). This result was also confirmed by Raman spectroscopy. The bands at 210, 275, 392, 483, 597 and 1322 cm^{-1} in Fig. 1b match those for the α-Fe_2O_3 phase [31]. Bands at 968 cm^{-1} and 1120 cm^{-1} may indicate other iron oxide

phases or iron sulfate residues. Figure 1c shows the UV-visible absorption spectrum of the haematite film. There was a broad band with two shoulders 300–480 nm and 480–600 nm. The electronic transition on the energy levels of the haematite can occur through a direct transition, corresponding to $O^{2-} \rightarrow Fe^{3+}$, and indirect transition between ions Fe^{3+} [32]. The UV-vis data were used to build Tauc plots by using Eq. 1:

$$(\alpha h\upsilon)^{\frac{1}{n}} = h\upsilon - E_g \qquad 1$$

where α is the absorption coefficient; $h\upsilon$ is the energy of a photon; E_g is the energy gap, in eV, between the valence and conduction band; and n is a constant, when assumed as $n = 2$ for indirect transition and $n = \frac{1}{2}$ for direct transition. The insert of the Fig. 1c shows the Tauc plot for haematite that presents a good linearity with $n = 2$ (corresponding to an allowed indirect electronic transition) and a band gap potential of 2.1 eV, which correspond to the theoretical value for haematite [33]. Tauc plot with $n = \frac{1}{2}$ (see Fig. S1) shows poor linearity excluding a direct electronic transition [32, 34]. Figure 1d–f shows a typical top view and cross-section SEM image of haematite film, which present a dense packed sphere-shaped nanostructure of particles with an average size of 30 nm. The cross-section view images show good adherence to the substrate and a film thickness of approximately 200 nm.

Fig. 1

a X-ray diffraction patterns, **b** Raman spectra, inset shows images of the fresh α-Fe_2O_3, **c** UV-vis and Tauc plot with $n = 2$ for indirect electronic transition and **d–f** SEM images of top-view (**d-c**) and **f** cross-section of α-Fe_2O_3

AQ4
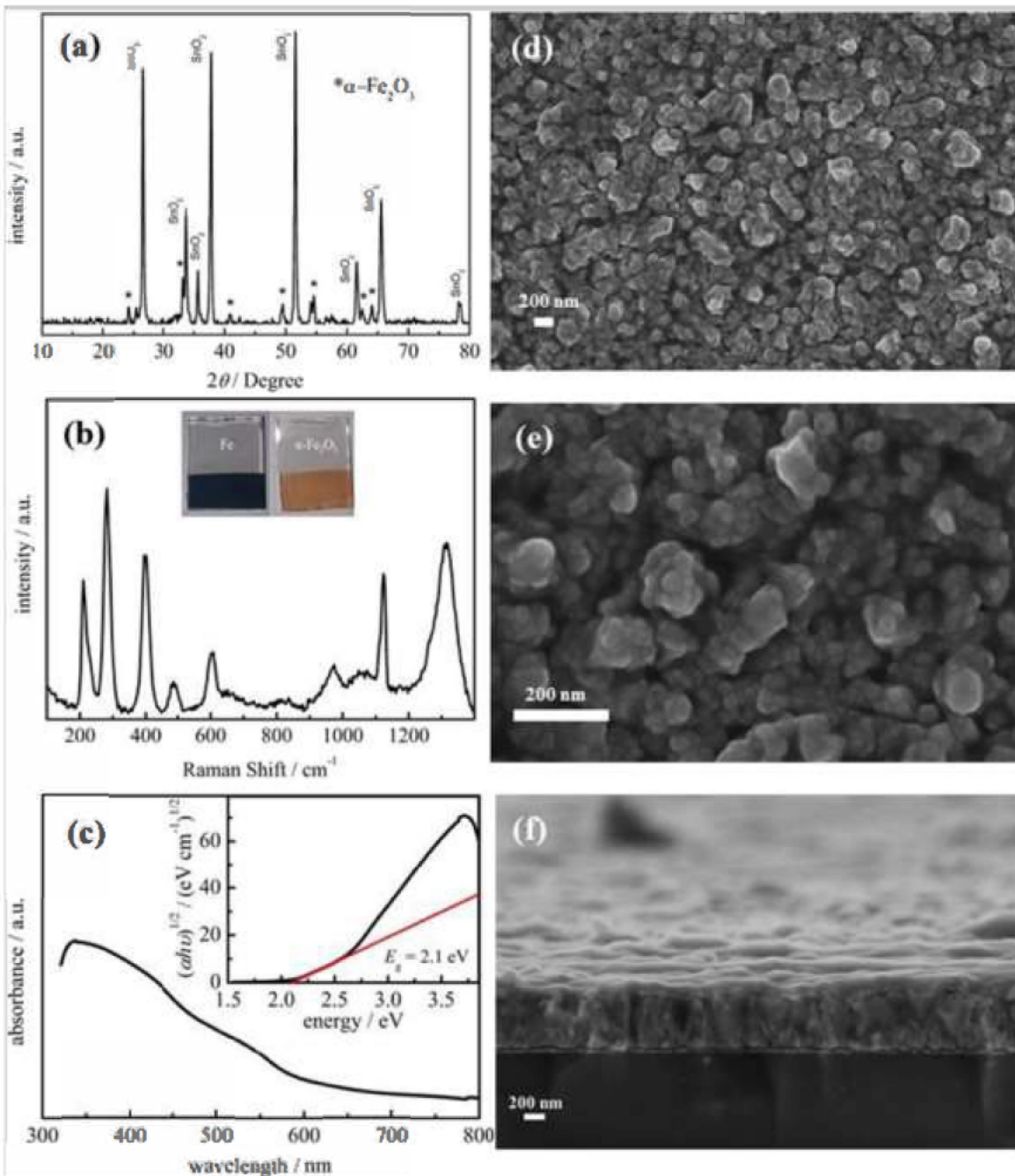
Photoelectrochemical oxidation water and glycerol

Figure 2a compares the photocurrents obtained in cyclic voltammetry experiments of the haematite film in both 0.1 M KOH and 0.1 M KOH + 1.0 M glycerol. Under illumination, the onset of water oxidation reaction is close to 0.95 V in agreement with previous studies [35, 36, 37]. On the other hand, in the presence of glycerol, higher photocurrents in potentials 400 mV lower than those for water oxidation are observed. Figure 2b shows the linear potential

sweep under chopped light condition. In the absence of glycerol, the photocurrents present spikes when the light is both turned on and off. The photocurrent has an exponential decay from those spikes and readily builds up a photocurrent value that matches with the constant illumination profile, which is associated to the hole-electron recombination at the semiconductor surface [38]. The intensity of the photocurrent spikes considerably decreases in the presence of glycerol and the photocurrent builds up at higher values, which indicates lower hole-electron recombination. Figure 2c shows the Mott-Schottky (MS) plot for the haematite photoanode in 0.1 M KOH. According to the MS analysis based on Eq. 2:

$$1/C^2 = 2/\varepsilon_r \varepsilon_0 A^2 e N_D \left(E - E_{fb} - kT/e \right) \qquad\qquad 2$$

Fig. 2

Cyclic voltammograms of haematite film at 0.05 V s ^{1} in the absence (black line) and in the presence of 0.10 M of glycerol (red line) under **a** continuum and **b** chopped illumination. **c** Mott-Schottky plot in the dark of the haematite film, capacitance measured at 1.0 kHz by impedance spectroscopy
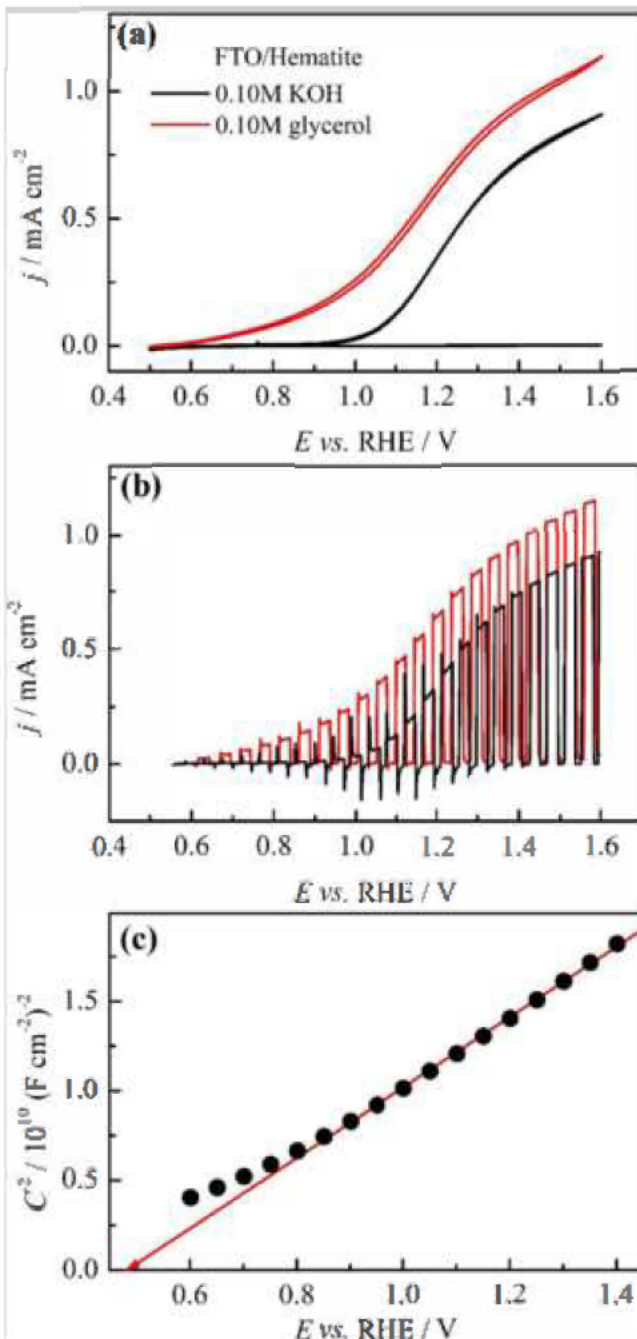
By the extrapolation of the linear curve ($R^2 = 0.999$), the intercept at $C^{-2} = 0$ released a 0.48 V flat band potential, E_{fb}, which is 0.47 V more negative than the photocurrent onset on blank solution in agreement with the literature [36]. The presence of glycerol shifts the onset photocurrent to 0.51 V that is 0.03 V more positive than the flat band potential estimated by MS analysis, see Fig. 2a. The positive slope of the curve C^{-2} versus E, Fig. 1c, is inversely related to the carrier density, N_D, of a n-type semiconductor, which gives a $N_D = 8.95 \times$

10^{19} cm ^{3} (calculus details are presented in the SI). The N_D value agrees with reported data for Si [39] and Sn [40] doped haematite and haematite thin films [24]. A trace of Si and Sn could not be excluded due to the nature of substrate, but as reported by Korjenic et al. [41], the carrier density for haematite, estimated in this work, is different for the N_D calculated for FTO in 0.1 M NaOH, around 1×10^{21} cm ^{3}, which suggest a full recovering of the haematite film as indicated by the SEM images presented in Fig. 1.

The temperature dependence of the GPECO by the haematite photoanode was investigated at different potentials, using both constant and chopped illumination. Regardless of the applied potential, in the 0.80–1.40 V range, the photocurrents increased with the temperature from 15 to 35 °C (see Fig. S2). The apparent activation energy, E_a, was calculated from the Arrhenius plots (Fig. 3a), and the results were the same for the constant and chopped light. Figure 3b shows that the E_a values decrease with the applied potential from 14 to 10 kJ mol ^{1}. We were not able to evaluate the E_a at potentials bellow 1.4 V in the absence of glycerol (blank solution), i.e., for the photoelectrooxidation of water (the details are presented in supplementary information, Fig. S3). However, the E_a at 1.4 V, was ca 3.0–4.0 kJ mol ^{1}, which is 3-folds smaller than that for the system containing glycerol. This indicates that the presence of glycerol at the interphase change the processes that determines the E_a.

Fig. 3

Temperature effect on GPECO on haematite. **a** Arrhenius plot for different applied potential regarding the chopped (open circle) and constant (full circle) illumination and **b** activation energy in function of applied potential, for GPECO (red full circles) and PEC water oxidation (black full circle)
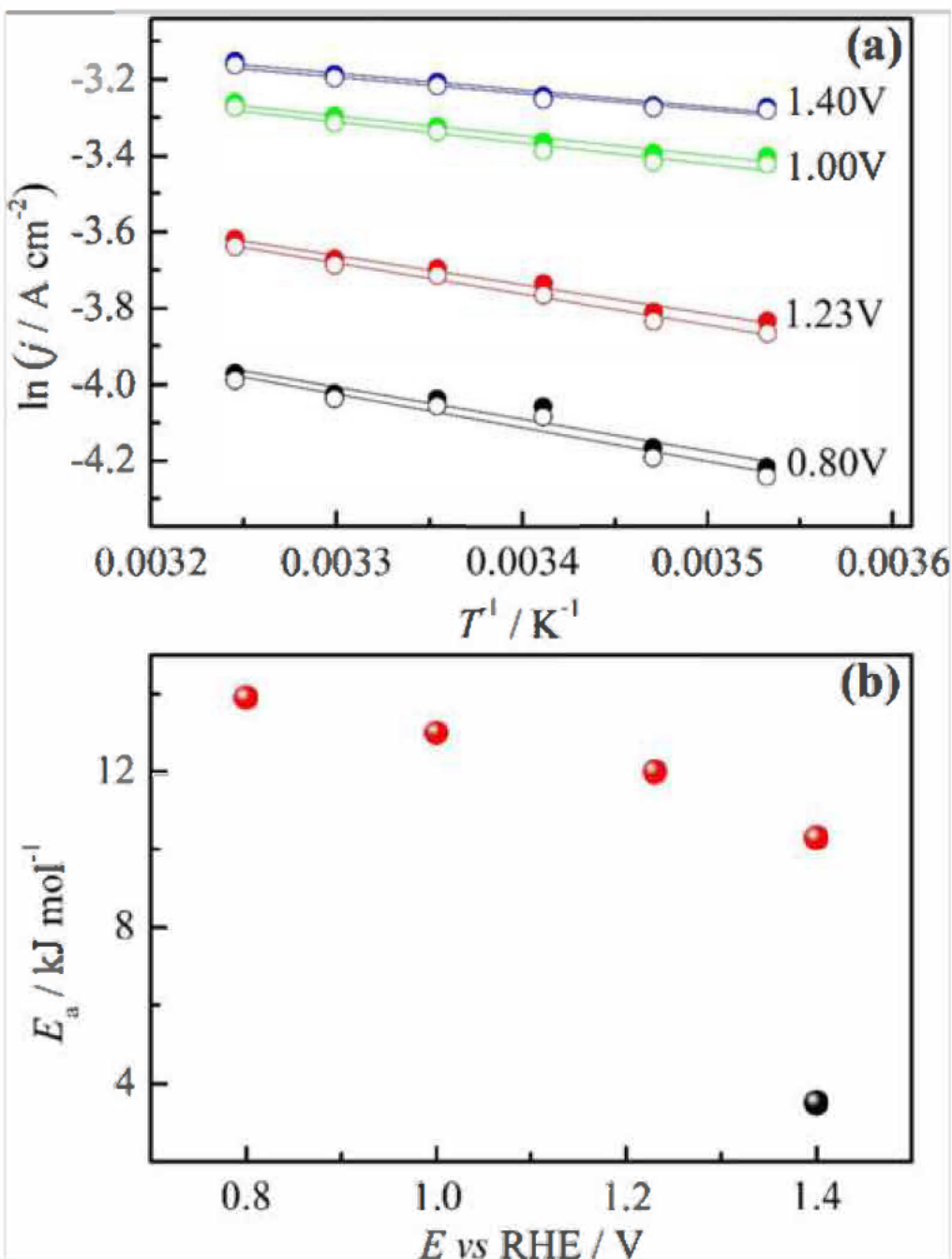
In situ FTIR and HPLC experiments

In situ FTIR spectra were performed in H_2O and D_2O. Figure 4 shows the results obtained in 1.0 M KOH and 0.1 M glycerol, prepared with D_2O (Fig. 4a) and H_2O (Fig. 4b), with tin-modified haematite. Fig. S4 presents the same experiment but in 0.1 M KOH and 0.1 M glycerol with haematite and tin-modified haematite. For a detailed discussion about the band assignment, see the main manuscript and the supporting information of the article recently

published by some of us [42]. The results in Fig. S4 are very similar to those in Fig. 4, except for the development of a band at 2343 cm^{-1} corresponding to the formation of CO_2 in the experiment using 0.1 M KOH, which is a consequence of the acidification of the thin layer. This issue is shared by all the techniques performed in the thin layer configuration and have been discussed in detail elsewhere [42, 43].

Fig. 4

In situ FTIR spectra recorded during the GPECO on GC/haematite with 3.5 wt% of tin under illumination of 455 nm LED light. **a** FTIR spectra acquired in D_2O electrolyte and **b** in H_2O. Electrolyte: 1.0 M KOH + 0.10 M glycerol
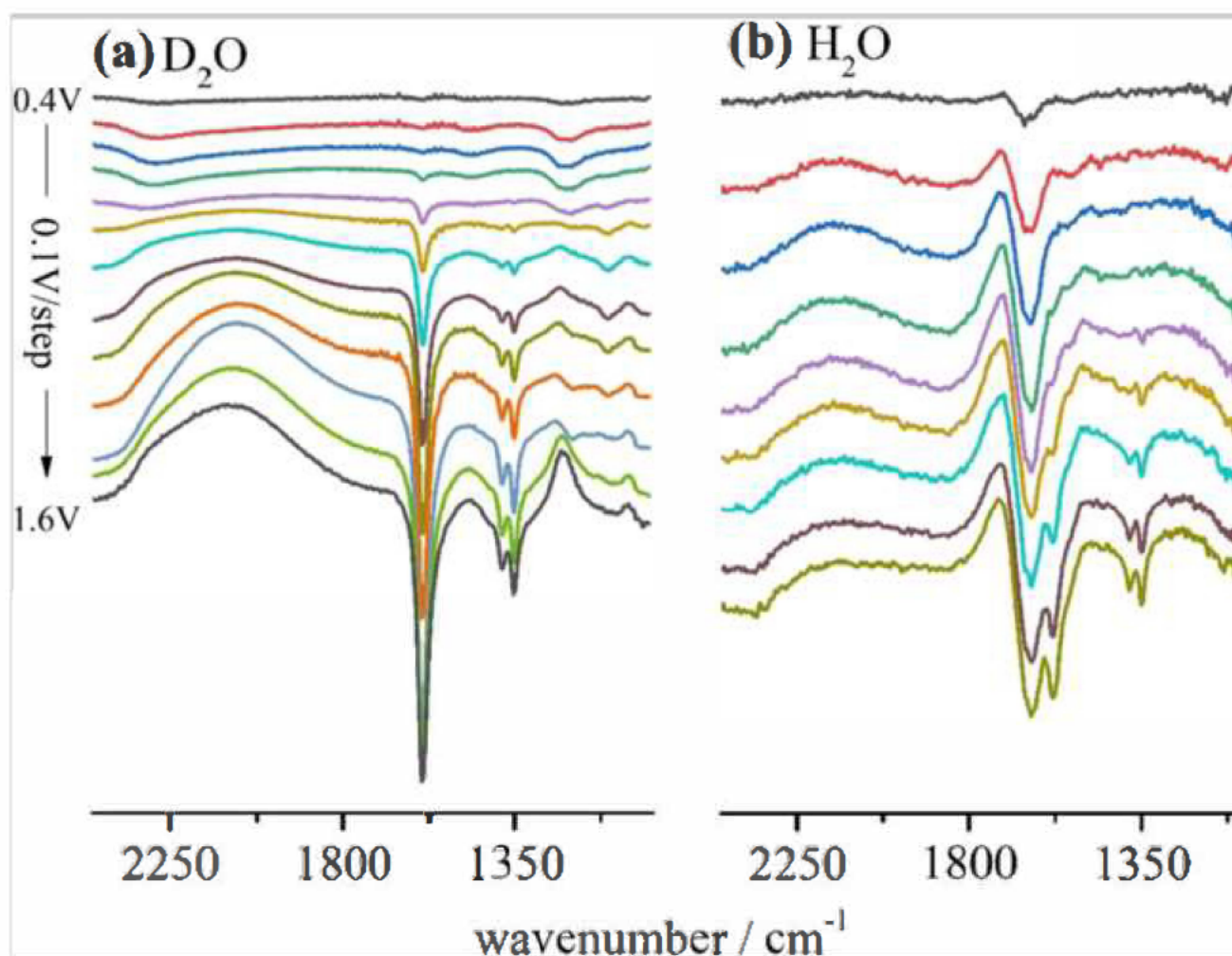

Figure 4a shows the development of three bands as a function of the applied potential. A double band at 1352 and 1380 cm^{-1} assigned to the formation of

formate and an intense band at 1580 cm^{-1} that may correspond to several compounds like formate, glycolate and glycerate ions. An interesting result is that independently of the KOH concentration the characteristic large band centred at 1400 cm^{-1}, due to the formation of CO_3^{2-} is absent (compare these results with those of references [42, 44, 45]), indicating that glycerol is completely oxidized only when the interfacial pH decreases. Experiments with D_2O permit to observe the development of bands between 1300 and 2000 cm^{-1} as this solvent does not interfere with the signal in this region. On the other hand, D_2O strongly absorbs the IR radiation in the region around 2000 cm^{-1} lowering the sensitivity of the method in this region. Thus, with the aim of monitoring if the pH of the thin layer turned acid under these conditions, we repeated the experiments shown in Fig. 4a in H_2O (Fig. 4b), because this solvent does not absorb the radiation at 2343 cm^{-1} permitting the eventual detection of CO_2. The results in Fig. 4b are similar to that shown in Fig. 4a, confirming the absence of CO_2 and, consequently, that the thin layer pH is alkaline during all the experiment.

The difference in these figures in the region around 1600 cm^{-1} is due to the disturbance generated by the absorption of H_2O in this region. In situ FTIR confirms the production of formate independently of the pH and the haematite modification. However, the band around 1580 cm^{-1} may have contributions coming from other substances containing carbonyl groups. To get deeper insight about the formation of product of the GPECO, we performed chronoamperometries and analyse the products using HPLC. Fig. S5 shows the results of the chronoamperometric experiments carried out at 1.0 V versus RHE. During this time, the photocurrent initial value decreased by 60%.

Figure 5 shows the distribution of the products acquired from the HPLC analysis. These data were extracted from the chromatograms in Fig. S6. The peak assignment was done by comparing the retention time of the peaks observed in our sample with that of several by-products of the glycerol oxidation (Fig. S7). The concentration was calculated using the calibration curve of Fig. S8. As shown in the Fig. 5, after 4 h of electrolysis, glycerate, glycolate, formate and lactate were detected. It is important to note that lactate is not directly produced by an electrochemical reaction. The reaction at the electrode surface can generate glyceraldehyde or DHA, which are in

equilibrium in alkaline media and are not stable, generating (among other substances) lactate. [45, 46, 47] This instability of glyceraldehyde and DHA in alkaline media is well-known in articles in the field of electrocatalysis [44, 47], and it should be taken into account in the discussions about selectivity to DHA under these conditions.

Fig. 5

Product concentration quantified by HPLC. Data were extracted from the chromatograms in Fig. S6, the peak assignment was done based on the retention times of several glycerol PEC oxidation products (Fig. S7) and the concentration was calculated using the calibration curves shown in Fig. S8
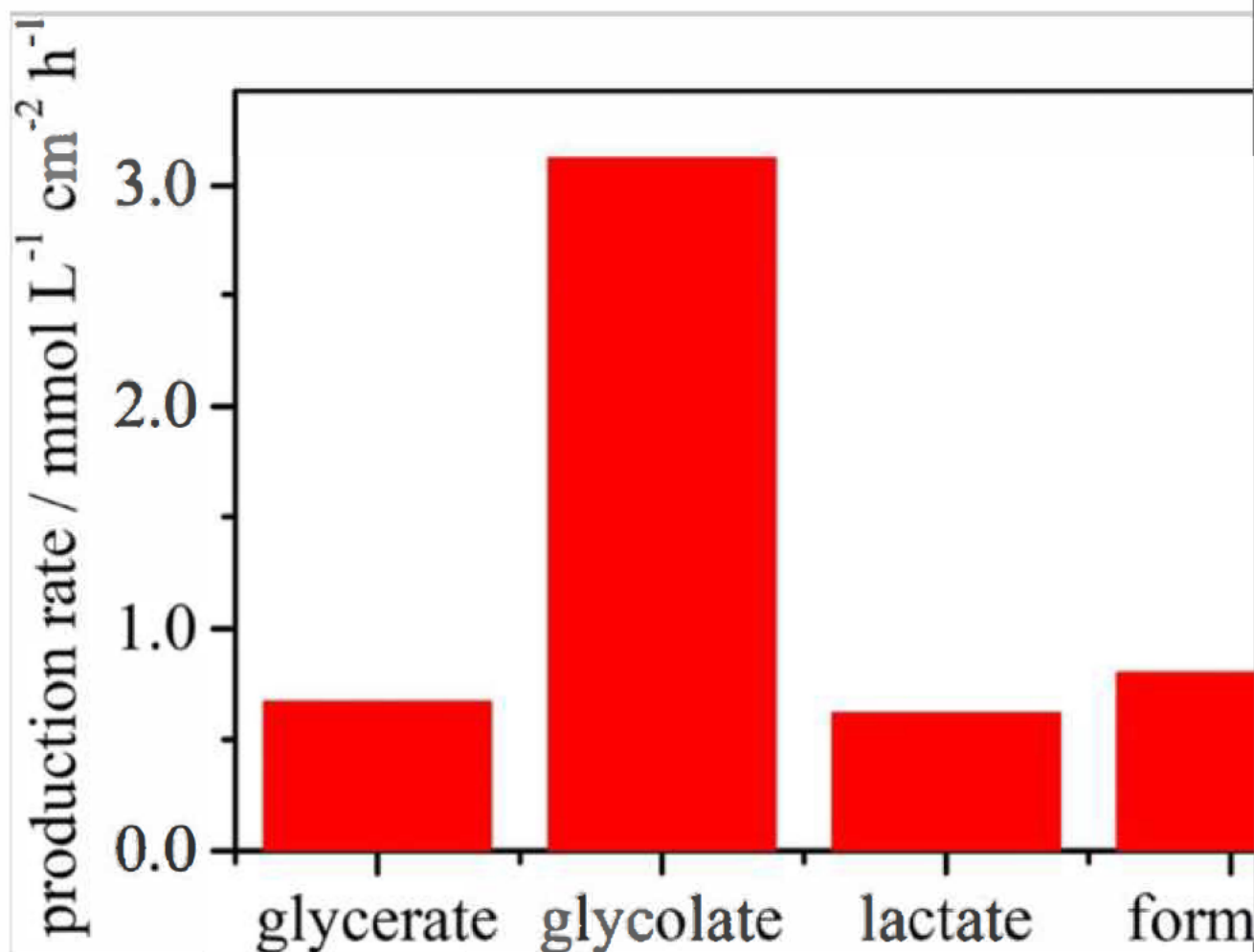
Discussion

Our electrochemical results show that adding glycerol to KOH increases the

electrooxidation current density and highly diminish the onset potential. Even though the (photo)electrooxidation of water has been extensively studied in this system [48], there are many fewer works about the PEC oxidation of organic molecules and the fundamental aspects of the reactions are almost completely unknown. However, results obtained with WO_3 [8] and TiO_2 [49] for the PEC of formic acid and with haematite for methanol [4], suggest that the reaction occurs through adsorption and subsequent oxidation into organic radicals on the photoanode surface. DFT studies [50] suggest the glycerol adsorption onto anatase TiO_2 (101) facilitates the formation of a hole in the terminated oxygen and this hole can be trapped in the glycerol molecule only if a dissociative deprotonation takes place.

The changes of photocurrents with the electrolyte temperature revealed that the apparent activation energy of the reaction is around 10–14 kJ mol ^{1} between 15 and 35 °C. Interestingly, these values are close to those reported for the glycerol electrochemical oxidation on noble metal oxides in alkaline media [51]. The E_a, at 1.4 V, in the base electrolyte was 3-fold smaller than GPECO. In the present work, the solution thermal effect was estimated by means of the changes on photocurrents at constant potentials; thus, it is important emphasizing that the applied potential acts on the separation of the photogenerated electron/hole pairs and while the electrons are collected by the external system, the holes are accumulated on the surface to then react with water or glycerol. As above mentioned, in the presence of small organic molecules, the reactions proceed via organic oxidation instead of oxygen evolution [8]. The photocurrent-temperature dependence is connected to the temperature influence on several interfacial processes on both, electrode and solution sides, namely: (i) the pair electron/hole formation and/or their mobility inside the haematite, (ii) the relative intermediates surface coverage and their reactivity, (iii) the glycerol diffusion from bulk to interface and (iv) a couple to three first points. At first sight, the low dependence of photocurrent with the temperature (E_a values) suggests the connection of this parameter with (i) or with the radicals formation/reaction as the RDS in (ii) (the high glycerol concentration employed allows us to exclude a mass transport limitation effect); however, once the chemical reaction at the interface is composed by several steps, the activation energy is not straightforward connected with the energy barriers in elementary steps [52]. Durrant et al. [37] showed that increasing the surface hole density,

the water oxidation reaction changes from first to third order with respect to the hole accumulation on the surface, suggesting a reaction mechanism involving three holes or oxidizing equivalents at the haematite surface. The same group also showed that the methanol oxidation to formaldehyde on haematite proceeding via adsorbed methoxy radicals is a second order reaction in respect to the hole accumulation on the surface in the whole potential window studied [4]. Based on the mechanism suggested by Durrant et al. for methanol oxidation [4], Fig. 6 shows one of the probable key intermediates for the glycerol photooxidation. The adsorbed radical intermediate is formed through the dehydrogenation of one of the –OH groups of the polyol. However, it is important to note that in alkaline media the reactive specie could be the ion glyceroate as already suggested by some of us for the electrochemical oxidation of glycerol on noble metals [42, 44, 45]. Irrespective of the active reactant origin, the intermediate will then react with other catalytic sites thought the C–H molecule bond scission to form one of the several possible reaction products of this complex reaction. The presence of several reaction products inferred by HPLC can be explained by two factors, namely: (1) several intermediates can be formed, for instance, glycerol can bind the surface through the –OH of the secondary carbon of through more than one –OH group, (2) as shown in Fig. 6 the high reactivity of the holes can generate multiple dehydrogenation in one or more carbons of the same intermediate or the attack to the C–C bond.

Fig. 6

One of the several likely intermediates for the photoelectrooxidation of glycerol. This organic radical, which binds to the Fe^{III} through the OH group, can react with the accumulated holes at the electrode surface in different ways generating one or more dehydrogenations and/or C–C bond breaking. This set of reactions possibilities and the presence or other C3 intermediates explain the presence of several products for this reaction
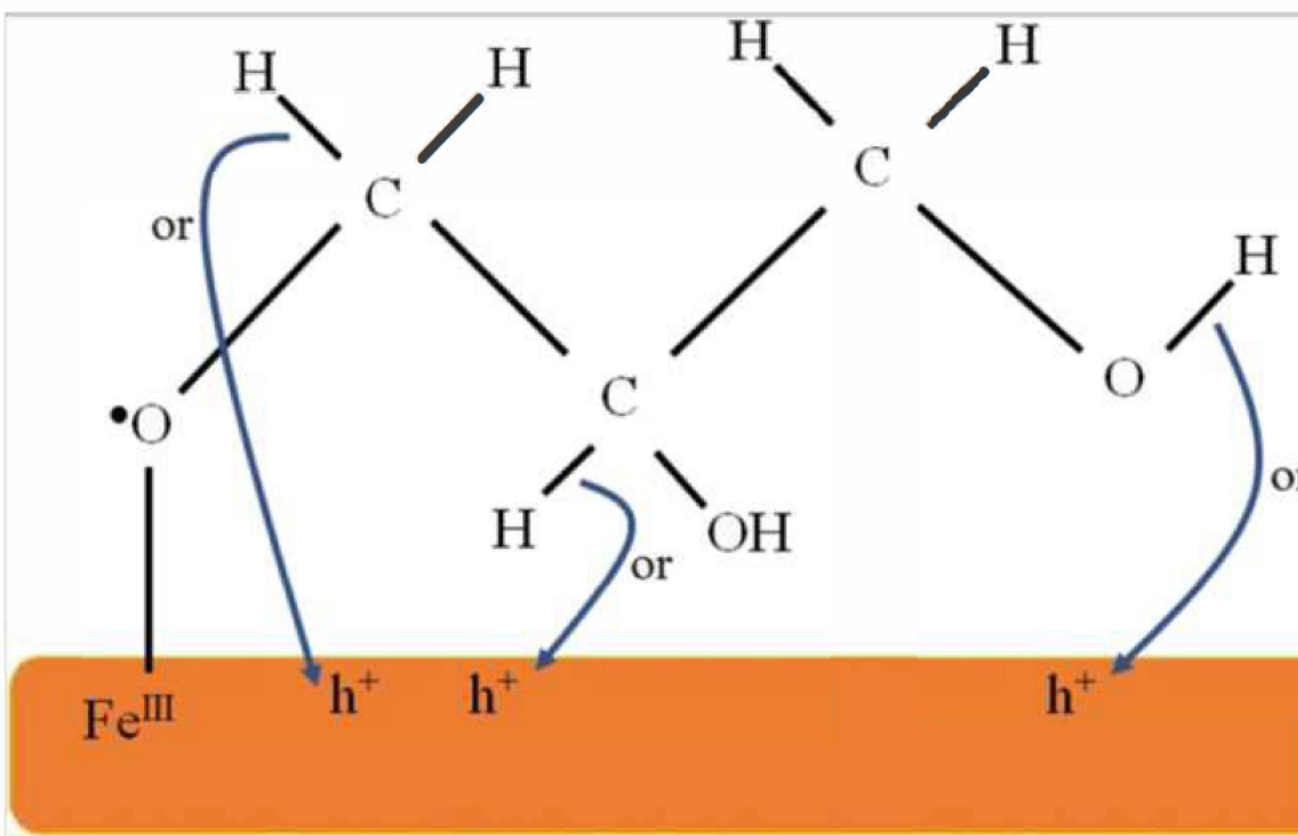
Finally, the *J* vs *E* curves in the absence and presence of glycerol and specially their changes with temperature are very distinct. For instance, while in the presence of glycerol, the potential of onset is not influenced by the temperature and regardless of the potential, the photocurrents increase with temperature, and in glycerol-free solution, the current decreases with temperature leading to an anti-Arrhenius behaviour at potentials lower than 1.3 V (Fig. S3). This phenomenon is only explained considering the coupling between several factors contributing to the E_a that will be explored in future works.

In situ FTIR and HPLC analysis permitted to detect and quantify the presence of C1, C2 and C3 products. These results are in line with those recently published by Liu et al. [20] and Chong et al. [28]. By using analytical techniques and computational experiments (DFT), the authors suggested that the GPECO on $BiVO_4$ occurs through a mechanism involving the adsorption of glycerol and intermediates on the catalyst and the formation of radicals. The high reactivity of radicals explains the low selectivity of the reaction, independently of the catalyst and the pH of the solution. In situ FTIR results showed that the haematite is able to completely break the C–C chain of the

alcohol producing formate (which was also detected by HPLC); however, we did not detect the presence of carbonate. On the other hand, another important aspect is the much higher quantity of lactate (2 carbons) than formate (1 carbon). If the molecule of glycerol is broken to form a lactate ion, then a C1 substance must be formed. Then, HPLC results suggest that 2 mmol L^{-1} cm^{-2} h^{-1} of CO$_3$$^{2-}$ was formed during the electrolysis (this ion cannot be detected in our HPLC system). It is worth to note that it is not a contradiction between in situ FTIR and HPLC results as these experiments are performed in completely different conditions. The long-term electrolysis (4 h) increases the probability for the products to diffuse to the electrode increasing their oxidation degree.

Conclusions

Haematite was synthesized using an easy and fast protocol involving the electrodeposition of lactate-iron complex in aqueous phase followed by thermal treatment. The incorporation of glycerol in the electrolyte generates higher currents at lower electrochemical potential, which means less cost in energy to produce hydrogen gas. In situ FTIR and electrolysis coupled to HPLC permit to determine the main product of the reaction, namely carbonate, formate, glycolate, glycerate and lactate, showing the low selectivity of the haematite photoanode. Previous results and our electrochemical studies at different temperatures suggest that the reaction occurs through a mechanism involving highly active radical intermediates, which also explain the low selectivity.

Publisher's note

Springer Nature remains neutral with regard to jurisdictional claims in published maps and institutional affiliations.

Acknowledgements

was also financed in part by the Coordenação de Aperfeiçoamento de Pessoal de Nível Superior - Brasil (CAPES) - Finance Code 001.

Compliance with ethical standards

Conflict of interest   There are no conflicts to declare.

Supplementary Information

ESM 1

(DOCX 1145 kb)

References

AQ5

1. Ibrahim N, Kamarudin SK, Minggu LJ (2014) Biofuel from biomass via photo-electrochemical reactions: an overview. J Power Sources 259:33–42

2. Pawar RC, Pyo Y, Ahn SH, Lee CS (2015) Photoelectrochemical properties and photodegradation of organic pollutants using hematite hybrids modified by gold nanoparticles and graphitic carbon nitride. Appl Catal B Environ 176–177:654–666

3. Li G, Wang C, Yan Y, Yan X, Li W, Feng X, Li J, Xiang Q, Tan W, Liu F, Yin H (2020) Highly enhanced degradation of organic pollutants in hematite/sulfite/photo system. Chem Eng J 386:124007

4. Mesa CA, Kafizas A, Francàs L, Pendlebury SR, Pastor E, Ma Y, le Formal F, Mayer MT, Grätzel M, Durrant JR (2017) Kinetics of photoelectrochemical oxidation of methanol on hematite photoanodes. J Am Chem Soc 139(33):11537–11543

5. Kalamaras E, Dracopoulos V, Sygellou L, Lianos P (2016) Electrodeposited Ti-doped hematite photoanodes and their employment for photoelectrocatalytic hydrogen production in the presence of ethanol. Chem

Eng J 295:288–294

6. Wang G, Ling Y, Lu X, Zhai T, Qian F, Tong Y, Li Y (2013) A mechanistic study into the catalytic effect of $Ni(OH)_2$ on hematite for photoelectrochemical water oxidation. Nanoscale 5(10):4129–4133

7. Shimura K, Yoshida H (2011) Heterogeneous photocatalytic hydrogen production from water and biomass derivatives. Energy Environ Sci 4(7):2467–2481

8. Reichert R, Zambrzycki C, Jusys Z, Behm RJ (2015) Photo-electrochemical oxidation of organic C1 molecules over WO_3 films in aqueous electrolyte: competition between water oxidation and C1 oxidation. ChemSusChem 8(21):3677–3687

9. Monllor-Satoca D, Borja L, Rodes A, Gómez R, Salvador P (2006) Photoelectrochemical behavior of nanostructured WO_3 thin-film electrodes: the oxidation of formic acid. ChemPhysChem 7(12):2540–2551

10. Lu X, Xie S, Yang H, Tong Y, Ji H (2014) Photoelectrochemical hydrogen production from biomass derivatives and water. Chem Soc Rev 43(22):7581–7593

11. Ru Ng AY, Boruah B, Chin KF, Modak JM, Soo HS (2020) Photoelectrochemical cells for artificial photosynthesis: alternatives to water oxidation. ChemNanoMat 6(2):185–203

12. Pagliaro M, Ciriminna R, Kimura H, Rossi M, Della Pina C (2007) From glycerol to value-added products. Angew Chemie Int Ed 46:4434–4440

13. Bagheri S, Julkapli NM, Yehye WA (2015) Catalytic conversion of biodiesel derived raw glycerol to value added products. Renew Sust Energ Rev 41:113–127

14. Martins CA, Fernández PS, Camara GA (2018) Alternative uses for

biodiesel byproduct: glycerol as source of energy and high valuable chemicals. Springer, Cham, pp 159–186

15. Coutanceau C, Baranton S, Kouamé RSB (2019) Selective electrooxidation of glycerol into value-added chemicals: a short overview. Front Chem 7:1–15

16. Ibadurrohman M, Hellgardt K (2020) Importance of surface roughness of TiO2 photoanodes in promoting photoelectrochemical activities with and without sacrificial agent. Thin Solid Films 705:138009

17. Bashiri R, Mohamed NM, Sufian S, Kait CF (2020) Improved photoelectrochemical hydrogen production over decorated titania with copper and nickel oxides by optimizing the photoanode and reaction characteristics. Mater Today Chem 16:100241

18. Seadira TWP, Masuku CM, Scurrell MS (2020) Solar photocatalytic glycerol reforming for hydrogen production over ternary cu/THS/graphene photocatalyst: effect of Cu and graphene loading. Renew Energy 156:84–97

19. Ravi P, Navakoteswara Rao V, Shankar MV, Sathish M (2020) CuO@NiO core-shell nanoparticles decorated anatase TiO_2 nanospheres for enhanced photocatalytic hydrogen production. Int J Hydrog Energy 45(13):7517–7529

20. Liu D, Liu J-C, Cai W, Ma J, Yang HB, Xiao H, Li J, Xiong Y, Huang Y, Liu B (2019) Selective photoelectrochemical oxidation of glycerol to high value-added dihydroxyacetone. Nat Commun 10(1):1779

21. Huang L-W, Vo T-G, Chiang C-Y (2019) Converting glycerol aqueous solution to hydrogen energy and dihydroxyacetone by the $BiVO_4$ photoelectrochemical cell. Electrochim Acta 322:134725

22. Souza FL (2018) Sunlight-driven water splitting using hematite nanorod photoelectrodes. An Acad Bras Cienc 90:745–762

23. Jiang C, Moniz SJA, Wang A, Zhang T, Tang J (2017) Photoelectrochemical devices for solar water splitting – materials and challenges. Chem Soc Rev 46(15):4645–4660

24. Muche DNF, dos Santos TMG, Leite GP, Melo MA Jr, Gonçalves RV, Souza FL (2019) Tailoring hematite/FTO interfaces: new horizons for spin-coated hematite photoanodes targeting water splitting. Mater Lett 254:218–221

25. Dharmadasa IM, Haigh J (2006) Strengths and advantages of electrodeposition as a semiconductor growth technique for applications in macroelectronic devices. J Electrochem Soc 153(1):G47

26. Jang JT, Ryu H, Lee WJ (2015) The growth of hematite by electrochemical deposition for PEC applications. J Alloys Compd 638:387–392

27. Liang P, Li L, Liu C, Wang W, Zhang H, Mitsuzaki N, Chen Z (2018) Effects of cathodic electrodeposition conditions on morphology and photoelectrochemical response of $\alpha\text{-}Fe_2O_3$ photoanode. Thin Solid Films 666:161–171

28. Chong R, Wang B, Li D, Chang Z, Zhang L (2017) Enhanced photoelectrochemical activity of nickel-phosphate decorated phosphate-Fe_2O_3photoanode for glycerol-based fuel cell. Sol Energy Mater Sol Cells 160:287–293

29. Bott-Neto JL, Rodrigues MVF, Silva MC, Carneiro-Neto EB, Wosiak G, Mauricio JC, Pereira EC, Figueroa SJA, Fernández PS (2020) Versatile spectroelectrochemical cell for in situ experiments: development, applications, and electrochemical behavior. ChemElectroChem 7(21):4306–4313

30. Shinde PS, Annamalai A, Kim JH, Choi SH, Lee JS, Jang JS (2015) Exploiting the dynamic Sn diffusion from deformation of FTO to boost the photocurrent performance of hematite photoanodes. Sol Energy Mater Sol

Cells 141:71–79

31. de Faria DLA, Lopes FN (2007) Heated goethite and natural hematite: can Raman spectroscopy be used to differentiate them? Vib Spectrosc 45(2):117–121

32. Cherepy NJ, Liston DB, Lovejoy JA, Deng H, Zhang JZ (1998) Ultrafast studies of photoexcited electron dynamics in γ- and α-Fe_2O_3 semiconductor nanoparticles. J Phys Chem B 102(5):770–776

33. Townsend TK, Sabio EM, Browning ND, Osterloh FE (2011) Photocatalytic water oxidation with suspended alpha-Fe_2O_3 particles-effects of nanoscaling. Energy Environ Sci 4(10):4270–4275

34. Iandolo B, Zhang H, Wickman B, Zorić I, Conibeer G, Hellman A (2015) Correlating flat band and onset potentials for solar water splitting on model hematite photoanodes. RSC Adv 5(75):61021–61030

35. Carvalho-Jr WM, Souza FL (2016) Thermal enhancement of water affinity on the surface of undoped hematite photoelectrodes. Sol Energy Mater Sol Cells 144:395–404

36. Tilley SD, Cornuz M, Sivula K, Grätzel M (2010) Light-induced water splitting with hematite: improved nanostructure and iridium oxide catalysis. Angew Chemie Int Ed 49(36):6405–6408

37. Le Formal F, Pastor E, Tilley SD et al (2015) Rate law analysis of water oxidation on a hematite surface. J Am Chem Soc 137(20):6629–6637

38. Rohloff M, Cosgun S, Massué C, Lunkenbein T, Senyshyn A, Lerch M, Fischer A, Behrens M (2019) The role of synthesis conditions for structural defects and lattice strain in β-TaON and their effect on photo- and photoelectrocatalysis. Zeitschrift für Naturforsch B 74(1):71–83

39. Cesar I, Sivula K, Kay A, Zboril R, Grätzel M (2009) Influence of feature size, film thickness, and silicon doping on the performance of

nanostructured hematite photoanodes for solar water splitting. J Phys Chem C 113(2):772–782

40. Ling Y, Wang G, Wheeler DA, Zhang JZ, Li Y (2011) Sn-doped hematite nanostructures for photoelectrochemical water splitting. Nano Lett 11(5):2119–2125

41. Korjenic A, Raja KS (2019) Electrochemical stability of fluorine doped tin oxide (FTO) coating at different pH conditions. J Electrochem Soc 166(6):C169–C184

42. de Souza MBC, Yukuhiro VY, Vicente RA, Vilela Menegaz Teixeira Pires CTG, Bott-Neto JL, Fernández PS (2020) Pb- and bi-modified Pt electrodes toward glycerol electrooxidation in alkaline media. Activity, selectivity, and the importance of the Pt atoms arrangement. ACS Catal 10(3):2131–2137

43. Jeffery DZ, Camara GA (2010) The formation of carbon dioxide during glycerol electrooxidation in alkaline media: first spectroscopic evidences. Electrochem Commun 12(8):1129–1132

44. De Souza MBC, Vicente RA, Yukuhiro VY et al (2019) Bi-modified Pt electrodes toward glycerol electrooxidation in alkaline solution: effects on activity and selectivity. ACS Catal 9(6):5104–5110

45. Lima CC, Rodrigues MVF, Neto AFM, Zanata CR, Pires CTGVMT, Costa LS, Solla-Gullón J, Fernández PS (2020) Highly active Ag/C nanoparticles containing ultra-low quantities of sub-surface Pt for the electrooxidation of glycerol in alkaline media. Appl Catal B Environ 279:119369

46. Lux S, Siebenhofer M (2013) Synthesis of lactic acid from dihydroxyacetone: use of alkaline-earth metal hydroxides. Catal Sci Technol 3(5):1380–1385

47. Birdja YY, Koper MTM (2017) The importance of cannizzaro-type reactions during electrocatalytic reduction of carbon dioxide. J Am Chem

Soc 139(5):2030–2034

48. Tamirat AG, Rick J, Dubale AA, Su WN, Hwang BJ (2016) Using hematite for photoelectrochemical water splitting: a review of current progress and challenges. Nanoscale Horizons 1(4):243–267

49. Reichert R, Jusys Z, Behm RJ (2014) A novel photoelectrochemical flow cell with online mass spectrometric detection: oxidation of formic acid on a nanocrystalline TiO_2 electrode. Phys Chem Chem Phys 16(45):25076–25080

50. Di Valentin C, Fittipaldi D (2013) Hole scavenging by organic adsorbates on the TiO_2 surface: a DFT model study. J Phys Chem Lett 4(11):1901–1906

51. Habibi E, Razmi H (2012) Glycerol electrooxidation on Pd, Pt and Au nanoparticles supported on carbon ceramic electrode in alkaline media. Int J Hydrog Energy 37(22):16800–16809

52. Mao Z, Campbell CT (2019) Apparent activation energies in complex reaction mechanisms: a simple relationship via degrees of rate control. ACS Catal 9(10):9465–9473

53. Schmidt KH (1977) Measurement of the activation energy for the reaction of the hydroxyl radical with hydrogen in aqueous solution. J Phys Chem 81(13):1257–1263